Industrial Crops & Products 210 (2024) 118149

Contents lists available at ScienceDirect

Industrial Crops & Products

journal homepage: www.elsevier.com/locate/indcrop

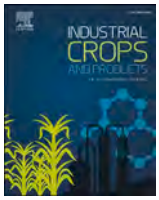

Hierarchical structure with dielectric/magnetic network from Kapok fiber with enhanced microwave attenuation capacity

Pengfei Zhao [a], Rui Wang [a], Jinlong Tao [a], Ximei Song [b,*], Yanfang Zhao [c], Jianhe Liao [c], Lusheng Liao [a,*], Zheng Peng [a]

[a] Guangdong Provincial Key Laboratory of Natural Rubber Processing, Agricultural Products Processing Research Institute, Chinese Academy of Tropical Agricultural Sciences, Zhanjiang 524001, China
[b] Zhanjiang Key Laboratory of Tropical Crop Genetic Improvement, South Subtropical Crops Research Institute, Chinese Academy of Tropical Agricultural Sciences, Zhanjiang 524013, Guangdong, China
[c] School of Materials Science and Engineering, Hainan University, Haikou 570228, China

ARTICLE INFO

Keywords:
Kapok fiber
Carbon microtube
Hierarchical structure
Electromagnetic coupling
Microwave-absorbing performance

ABSTRACT

Construction of hierarchical structures with dielectric and magnetic lossy blocks is a robust approach for fabricating functional materials with strong attenuation capacity over a broad range of frequencies. Herein, ultralight three-dimensional (3D) architecture with zero-dimensional (0D) cobalt ferrite-anchored two-dimensional (2D) carbon microtube ($CoFe_2O_4$ @CMT) was fabricated from Kapok fibers via facile solvothermal and subsequent pyrolysis methods. Such hierarchical structures with CMT as dielectric components and $CoFe_2O_4$ as magnetic blocks provide hybrids with improved microwave-absorbing capability. $CoFe_2O_4$ @CMT hybrid with a $CoFe_2O_4$/CMT mass ratio of 1:1 demonstrates a minimum reflection loss (RL) of − 66.78 dB at the thickness of 4.6 mm together with an effective absorption bandwidth (RL ≤ −10 dB) of 4.80 GHz. Moreover, over 90% of the electromagnetic energy ranging from 3.04 GHz to 18.00 GHz can be dissipated by expediently adjusting the thickness. Detailed investigation reveals that hierarchical structures with synergetic effects from dielectric CMT and magnetic $CoFe_2O_4$ efficiently tune impedance matching and attenuation capacity of the resulting $CoFe_2O_4$ @CMT, affording high microwave absorption performances. This work promises great potential in developing microwave absorbers starting from sustainable natural hollow templates.

1. Introduction

While the proliferation of wireless technologies devices and high-power telecommunication contribute to improving the quality of our life, omnipresent electromagnetic pollution from interference and radiation detrimentally impacts both human health (Wongkasem, 2021) and the reliability of sensitive equipment (Lv et al., 2022). To minify this inevitable issue, mara-ton of efforts have been dedicated to developing microwave-absorbing materials (MAMs) that are capable of attenuating hazardous electromagnetic energy by transferring it into internal energy (Pang et al., 2021). Traditional MAMs based on metals or metal oxides suffer from several shortcomings, including high density, poor chemical resistance, and narrow absorbing bandwidth. Therefore, researchers continuously explore innovative solutions to overcome these challenges and fabricate highly efficient MAMs that can absorb electromagnetic radiation over a broad frequency range. Owing to their lightweight, remarkable chemical resistance, and fascinating electrical properties, carbon materials have been deemed as one of the most perspective dielectric MAMs and captured considerable attention from academia and industry (Meng et al., 2018; Ren et al., 2014; Zhi et al., 2021). Nevertheless, developing carbon-based MAMs with efficient absorption over a broad frequency range remains challenging because of their inferior impedance matching and limited dielectric loss.

As is well-known, desired microwave-absorbing properties are mainly associated with balanced impedance matching and attenuation capacity, ascribing to the electromagnetic loss networks derived from dielectric or/and magnetic components (Zeng et al., 2020). To improve the microwave attenuation capacity of carbonaceous MAMs, various hierarchical structures (films, foams, aerogels, etc.) have been developed from low-dimensional nano-blocks by adopting appropriate component engineering and rational morphology design (Sharma and James, 2021; Wang et al., 2020a; Yu-Rui et al., 2022). For instance,

* Corresponding authors.
E-mail addresses: ximeisongjiayou@126.com (X. Song), lsliao@catas.cn (L. Liao).

https://doi.org/10.1016/j.indcrop.2024.118149
Received 7 August 2023; Received in revised form 19 October 2023; Accepted 22 January 2024
Available online 30 January 2024

CeO_2 (Wang et al., 2018b), Fe_3O_4 (Liu et al., 2019b), and Ni (Zheng et al., 2020) nanoparticles have been successfully anchored on carbonaceous materials for enhancing microwave-absorbing performances. Unlike zero-dimensional nanoparticles and two-dimensional nanosheets, one-dimensional (1D) nanoblocks demonstrate dramatic potential in forming electromagnetic loss networks with low percolation thresholds due to their unique shape anisotropy and effective charge transmission (Huang et al., 2020; Sharma and James, 2021). Among them, 1D hollow structures with the capability of generating multiple scattering/reflections have been regarded as promising candidates to tackle the high-density issue from magnetic dosing (Han et al., 2022; Huang et al., 2012). To reduce the weight of radar-oriented microwave absorbers, Xie and co-workers fabricated hollow carbon from polyacrylonitrile fibers using atmospheric thermo-oxidative stabilization and nitrogen-protect carbonization, demonstrating a minimum reflection loss (RL_{min}) of − 21.36 dB as well as an effective absorption bandwidth (EAB) of 2.88 GHz (Xie et al., 2008). Similarly, customizing heterointerfaces in hollow structures can boost polarization loss due to the presence of large surfaces area and abundant heterojunctions (Huang et al., 2016; Xu et al., 2022a). Chen et al. reported the fabrication of 1D electromagnetic-gradient TiO_2 @Co/C@Co/Ni multilayered microtubes by using coaxial electrospinning together with a solvothermal strategy, which exhibits excellent microwave attenuation capacity that is derived from the synergetic effects of structural anisotropy and multiple loss mechanisms (Jin et al., 2021). It has been proven that 1D hollow carbon derivates show high microwave attenuation capacity over broad frequencies (Bao et al., 2021; Jin et al., 2021). However, the unsustainable precursors, complicated fabrication, and economic unaffordability make them unfavorable for practical applications.

Alternatively, natural biomass-derived carbon as a promising absorbing material is capturing more and more attention not only because of its intrinsic merits of sustainability, environment-friendly, and vast resources but also due to its elaborate hierarchical structures and patterned metabolic microchannels (Zhao et al., 2019; Zhou et al., 2020). Apart from three-dimensional (3D) biomass-derived porous carbon, various 1D carbon from natural fibers have served as advanced sustainable MAMs (Song et al., 2022). Using 1D natural fibers as a template or precursor can inherit its hierarchical structures and hold the unique fiber shape (Li et al., 2019). Zhao et al. obtained Fe_3O_4-immobilized carbon nanofibers using natural collagen fibers as the templates, achieving an RL_{min} of 36.00 dB at 12.00 GHz and an EAB of 5.40 GHz (Wang et al., 2015). Similarly, Ji and co-workers fabricated a carbon cotton/Co@nanoporous carbon via a facile sintering technique, achieving an RL_{min} of − 51.20 dB over Ku-band (12.00–18.00 GHz) and a broad EAB of 4.40 GHz (Zhao et al., 2018), indicating that compounding traditional magnetic components with solid biomass-derived carbon fibers would benefit its intrinsic lightweight advantage. Notably, biomass with hollow structures has been confirmed to be a good choice for reducing effective permittivity, affording excellent impedance matching (Wu et al., 2018). Significant progress has been made in creating ultralight functional materials from hollow biomass, extending their application from dehumidification to adsorption, and catalyst carriers, super-thermal insulators, energy storage substances, and solar steam generators (Sun et al., 2021).

Owing to its hollow structure with an out diameter dozens of micrometers and a wall thickness of several micrometers, kapok fiber (KF) has been extensively developed as carbon microtube (CMT) for the application of absorbents, supercapacitors, catalysis, and so on (Zheng et al., 2021). Our previous works have confirmed that the KF can be a precursor for developing ultralight MAM with strong attenuation capacity over a wide frequency range (Zhao et al., 2022). Herein, $CoFe_2O_4$ was immobilized on KF-derived CMT via a facial hydrothermal approach followed by carbonization to further demonstrate the critical role of heterointerface engineering. Due to the 3D hierarchical structures-induced multiple scatterings/reflections and heterogenous networks-derived multiple loss mechanisms, the as-fabricated $CoFe_2O_4$ @CMT show an RL_{min} of − 66.78 dB at 16.48 GHz and an optimized EAB of 4.80 GHz. This work opens further avenues of fabricating biomass-derived hierarchical structures to facilitate microwave attenuation, providing deep insight into the correlation of composition-morphology-property.

2. Experimental section

2.1. Materials

KF was harvested from kapok trees (Bombax ceiba L.) planted in the South Subtropical Crops Research Institute, Chinese Academy of Tropical Agricultural Sciences, China. Sodium hypochlorite ($NaClO_2$, 80%), Cobalt (II) nitrate hexahydrate ($Co(NO_3)_2{\cdot}6\ H_2O$, > 99.99%), iron (III) nitrate nonahydrate ($Fe(NO_3)_3{\cdot}9\ H_2O$, > 99.99%), ethylene glycol (EG, >99.8%), ethanol (EtOH, >95%), and ammonium hydroxide ($NH_3{\cdot}H_2O$, 25%) were bought from Sinopharm Chemical Reagent Co. Ltd., China. Argon with a purity of 99.99% was provided by the Zhanjiang Oxygen Factory, China.

2.2. Preparation of $CoFe_2O_4$ @CMT

To create a hydrophilic and positively charged surface, the as-harvested KF was treated with 5.00 wt% $NaClO_2$ solution at 80 °C for 1 h, followed by rinsing with water and vacuum drying at 80 °C for 24 h. Meanwhile, $Co(NO_3)_2{\cdot}6\ H_2O$ (6.20 g) and $Fe(NO_3)_3{\cdot}9\ H_2O$ (17.22 g) were dispersed with ethylene glycol/water (v/v=1:1) to form a stock solution (300 g), whose concentration can be controlled by diluting. The $CoFe_2O_4$ @CMT was prepared via a hydrothermal reaction followed by carbonization. Typically, 1.00 g KF was impregnated entirely with 60.00 g precursors solution, accompanied by magnetically stirring at 80 °C for 2 h. After charging $NH_3{\cdot}H_2O$ (5.00 g) was charged, the suspension was transferred into a Teflon-lined hydrothermal reactor (100 mL) and kept at 200 °C for 12 h, affording $CoFe_2O_4$-anchored KF ($CoFe_2O_4$ @KF). After cooling to room temperature, the $CoFe_2O_4$ @KF was purified several times with ethanol and vacuum dried at 80 °C for 24 h. Finally, the as-dried product was annealed in a tube furnace at 600 °C for 2 h with a ramp rate of 10 °C, accompanying with Argon flow, affording black $CoFe_2O_4$ @CMT aerogels. For comparison, CMT, $CoFe_2O_4$, and $CoFe_2O_4$ @CMT-x (x represents the mass ratio of $CoFe_2O_4$ and CMT) were also fabricated according to the same procedure by simply adjusting the concentration of precursors.

2.3. Characterization

X-ray diffraction spectra (XRD) were collected with a Bruker D8 advanced diffractometer equipped with a Cu-Kα source (λ = 0.15406 nm). Raman patterns were collected on a HORIBA LabRAM HR Evolution Raman spectroscopy with a laser excitation source of 532 nm. X-ray photoelectron spectroscopy (XPS) was carried out using a Shimadzu Kratos Axis Ultra-DLD system with a monochromatic Al Kα X-ray source. Morphology and structure were examined by an Hitachi S-4800 scanning electron microscopy (SEM) with a Oxford Ultim Max energy dispersive spectroscopy and a FEI Tecnai G2 F30 high-resolution transmission electron microscopy (HRTEM), respectively. Electromagnetic parameters were collected using an Agilent N5230C vector network analyzer in transmission-reflection mode, with a frequency range of 2–18 GHz. Priority to measurement, the as-prepared sample powder was incorporated with paraffin in a mass concentration of 50% and then compressed into toroidal rings (3.04 mm in inner diameter, 7.00 mm in outer diameter, and 2.00 mm in thickness).

3. Results and discussion

Typically, top-down strategies which incorporate multifunctional

guests into the natural hollow fiber with multi-scale structures are versatile to scale-up fabricate tubular functional materials. Previously, various natural hollow fibers (e.g., gigantea, catkin, pappi of S. oleraceus L, and Milkweed) have been used as economic bio-template to prepare carbon microtubes and thereafter relevant hybrids (Sun et al., 2021). Herein, kapok fiber (KF) collected from kapok trees (Bombax ceiba L.) as natural templates was hybridized with magnetic components by hydrothermal reaction and subsequent carbonization, affording the successive precipitation of salt, crystallization of precursors, or heterogenous hybrids. Fig. 1 schematically illustrates the synthesis process for $CoFe_2O_4$ @CMT hybrids. Briefly, $NaClO_2$-treated KFs with a hydrophilic surface were added to an ethylene glycol/water solution containing $Co(NO_3)_2$ and $Fe(NO_3)_3$, where precursors (Co^{2+}, Fe^{3+}) will interact with oxygen groups (-OH, -COOH, etc.) on KF surface under the driving force of electrostatic attractions (Wang et al., 2014). With the presence of $NH_3{\cdot}H_2O$, $CoFe_2O_4$ @KF hybrids were gradually form via the co-precipitation of Co^{2+} and $Fe^{3+}$and in-situ growth of $CoFe_2O_4$ during the hydrothermal reaction. Finally, the as-dried $CoFe_2O_4$ @KF hybrids are further calcined at high temperature for the carbonization of KF, affording aerogels of $CoFe_2O_4$ @CMT with a bit of volume shrinkage. It is observed that the original fibers are white and have a round cross-section with a large lumen and thin wall, and the color of the sample turns to light brown and black over the following hydrothermal reaction and carbonization. Owing to the rigid nature of inorganic CMT, the obtained hierarchical $CoFe_2O_4$ @CMT hybrids inherit the porous structure, which can be simplified as porous aerogels with three-dimensional hollow skeletons as hosts and air as guests. Such hierarchical structures are propitious to decreasing the density and the effective permittivity, thus affording an excellent impedance matching condition (Zhao et al., 2019). As depicted in Fig. 1, KF-derived CMT in resulting hybrids maintain intact hollow fiber structure without severe breaking or collapsing, which can steadily stand on the top of a green leaf without causing severe deformation.

XRD spectra of CMT, $CoFe_2O_4$, and $CoFe_2O_4$ @CMT hybrids were performed to reveal the crystalline structure. As displayed in Fig. 2a, two broad diffraction peaks of CMT at $2\theta = 22.75^\circ$ and 44.64° are respectively ascribed to its (002) and (100) crystalline plane, indicating the formation of graphitic carbon during the annealing process, albeit with disorders (Song et al., 2020). The diffraction peaks at $2\theta = 18.26^\circ$, 30.11°, 35.47°, 43.11°, 53.45°, 56.98°, 62.57° and 65.47° belong to the crystalline planes of (111), (220), (311), (400), (422), (440), (511), and (533) for face-centered cubic spinel $CoFe_2O_4$ nanoparticles (JCPDS No.22–1086), respectively (Cui et al., 2019). Based on Scherrer's formula, average crystallite sizes of $CoFe_2O_4$ particles can be calculated to be about 20 nm, suggesting the nanocrystalline characteristics of $CoFe_2O_4$ (Xu et al., 2022b). Compared with CMT and $CoFe_2O_4$, $CoFe_2O_4$ @CMT hybrids exhibit all major diffraction peaks of cubic spinel $CoFe_2O_4$, implying that the $CoFe_2O_4$ was successfully anchored to CMT. Nevertheless, owing to the high scattering of wrapped $CoFe_2O_4$ and weak crystallinity of CMT, the characteristic peaks assigned to the (002) and (110) planes of CMT are barely observed in the patterns of $CoFe_2O_4$ @CMT hybrids. Carbon components and defects in the hybrids are crucial to microwave conductivity and dielectric loss, which is investigated by Raman spectroscopy. From Raman shifts of CMT and its hybrids presented in Fig. 2b, characteristic peaks around 1320 cm^{-1} and 1590 cm^{-1} are assigned to D-band and G-band of CMT, originating from the vibration of sp^3 defects or lattice distortion and the in-plane sp^2 carbon vibration, respectively(Wang et al., 2018b). Furthermore, the intensities ratio of the D-band to the G-band (I_D/I_G) is calculated to analyze the structural order degree concerning a perfect graphitic CMT in hybrids. It can be seen that I_D/I_G gradually declines with the increase of $CoFe_2O_4$, meaning the enhanced carbonization degree due to the catalytic effect (Fang et al., 2017). Values of I_D/I_G for $CoFe_2O_4$ @CMT hybrids were determined to be around 1.17–1.34, which is smaller than that of the CMT (1.38). The reduced I_D/I_G values imply that a large number of structural defects and disorders are restored after the pyrolysis, which is favorable for a higher conduction loss and subsequently enhanced microwave attenuation of the absorbers (Geng et al., 2023).

XPS was further performed to study the chemical valence states and bonding nature of $CoFe_2O_4$ @CMT-1, which is depicted in Fig. 3. As anticipated, there are apparent differences between the peak positions shown in Fig. 3a, where the coexistence of C 1 s at 285.08 eV, O 1 s at 532.08 eV, Fe 2p at 711.08 eV and Co 2p at 781.08 eV in the survey spectrum of $CoFe_2O_4$ @CMT-1 confirms the successful immobilization of $CoFe_2O_4$ onto the surface of CMT. In addition, the C, O, Co, and Fe atomic concentration in $CoFe_2O_4$ @CMT-1 (Fig. 3b) is 88.72%, 8.98%, 0.73%, and 1.57%, respectively. Remarkably, the atomic ratio of the ion is approximately 2, suggesting the presence of $CoFe_2O_4$. By the Gaussian fitting, the high-resolution C 1 s, O 1 s, Co 2p, and Fe 2p spectra are further described in Fig. 3c-f, respectively. The C 1 s spectrum of

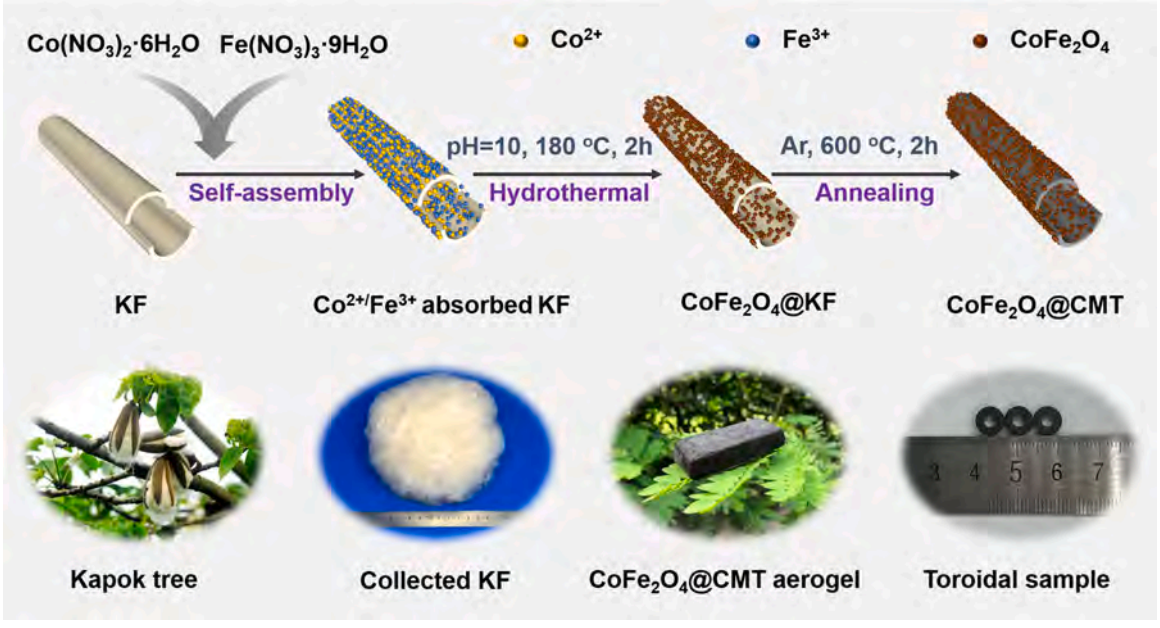

Fig. 1. Schematic illustration for the fabrication procedure of $CoFe_2O_4$ @CMT hybrids and digital photos of CMT and $CoFe_2O_4$ @CMT hybrids.

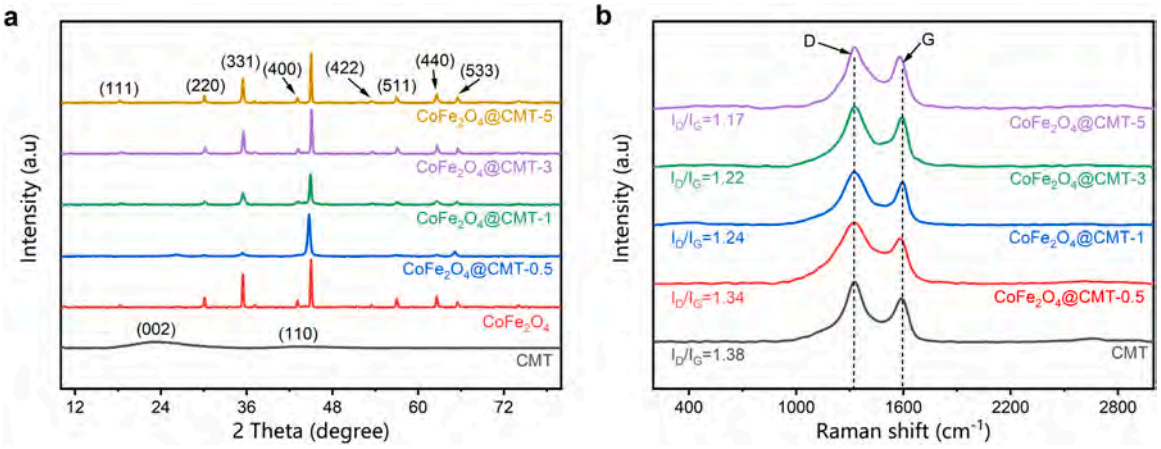

Fig. 2. (a) XRD spectra and (b) Raman shifts of CMT, $CoFe_2O_4$, and $CoFe_2O_4$ @CMT hybrids with different components.

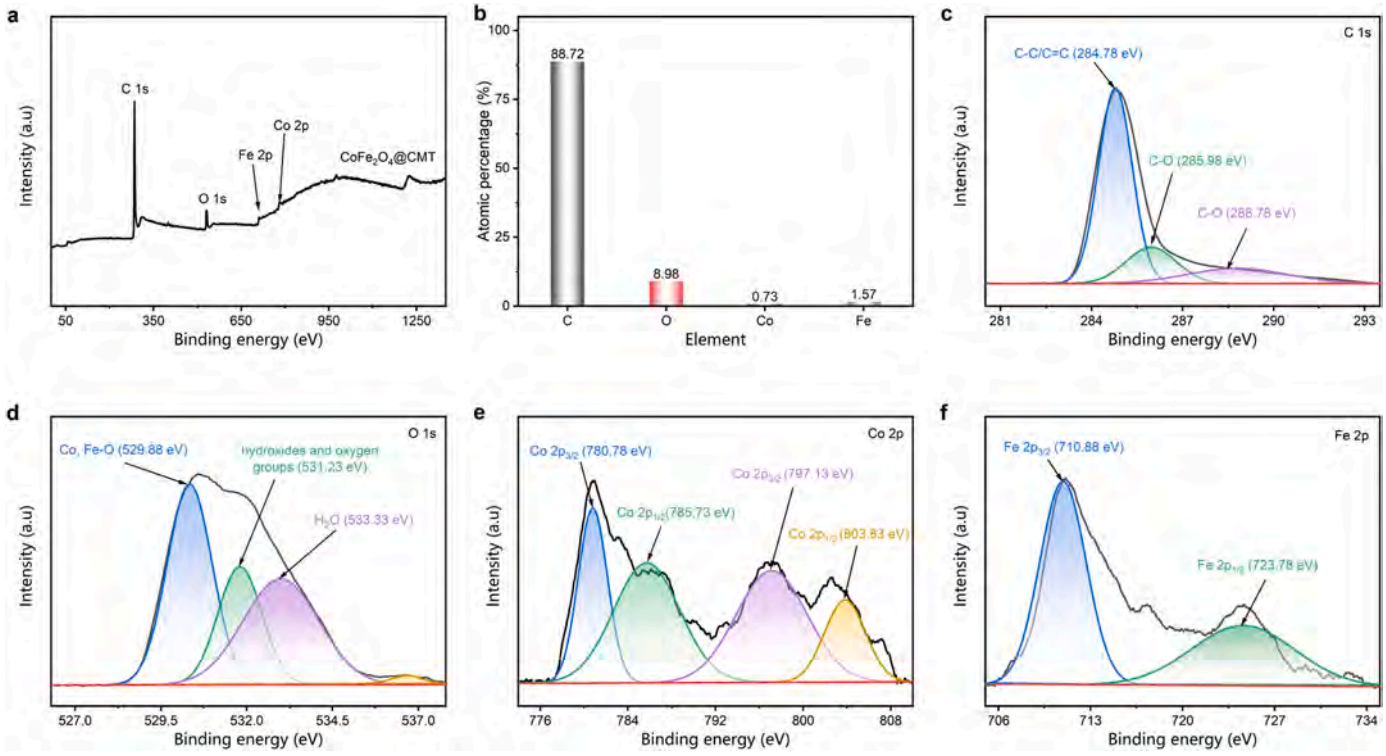

Fig. 3. XPS spectra of $CoFe_2O_4$ @CMT-1: (a) survey scan and spectra of (b) C1s, (c) O1s, (d) Co 2p and (e) Fe 2p.

$CoFe_2O_4$ @CMT-1 in Fig. 3c consists of three fitting peaks at 284.78 eV, 285.98 eV, and 288.53 eV, ascribing to C−C/C=C, C−O, and C=O, respectively. As the O 1 s spectrum shown in Fig. 3d, two prominent peaks with binding energies around 530.4 eV and 531.8 eV are attributed to the oxygen vacancies in $CoFe_2O_4$ and oxygen-containing groups (-OH and -COOH) of CMT, implying that there are some defects that are conducive to polarization loss (Geng et al., 2023). These vacancies and oxygen groups contribute to micro attenuation by acting as polarization centers. The Co 2p spectrum yields two peaks at 803.83 and 780.78 eV in (Fig. 3e), originating from Co $2p^{1/2}$ and Co $2p^{3/2}$, respectively. Evidenced by the 20.05 eV difference in binding energy, Co ion in the bivalent formal oxidation state is obtained, indicating the formation of Co in the standard spinel $CoFe_2O_4$ (Xu et al., 2022b). Furthermore, Fe $2p^{3/2}$ and Fe $2p^{1/2}$ with a binding energy difference of 13.70 eV further confirms the presence of Fe^{3+} in $CoFe_2O_4$ @CMT-1, which is consistent with the results in previous works (Xu et al., 2019).

Microstructures and morphologies of $CoFe_2O_4$, CMT, and $CoFe_2O_4$ @CMT were visualized by SEM together with an EDS. As shown in Fig. 4a, the obtained $CoFe_2O_4$ shows a chain architecture with packed grains of ~ 100 nm, implying that the carbon component as a template is indispensable for producing hierarchical structures. Furthermore, the controlled CMTs (Fig. 4b) demonstrate an original hollow tubular structure with a straight and smooth surface, of which the average thickness and diameter are about 1.36 μm and 30.42 μm, respectively. Such 1D hollow tubes can afford low-density and plentiful interfaces, which is in favorable to enhancing impedance matching and microwave attenuation. $CoFe_2O_4$ @CMT (Fig. 4c) displays hierarchical structures with $CoFe_2O_4$ nanocrystals as double shells and CMT as interlayer. Like XPS results, ths EDS elemental mapping of $CoFe_2O_4$ @CMT depicted in Fig. 4d disclose the distribution of C, O, Co, and Fe elements with the atomic Co/Fe of nearly 1/2, verifying the successful formation of $CoFe_2O_4$-anchored 1D hollow CMT. Additionally, TEM was further

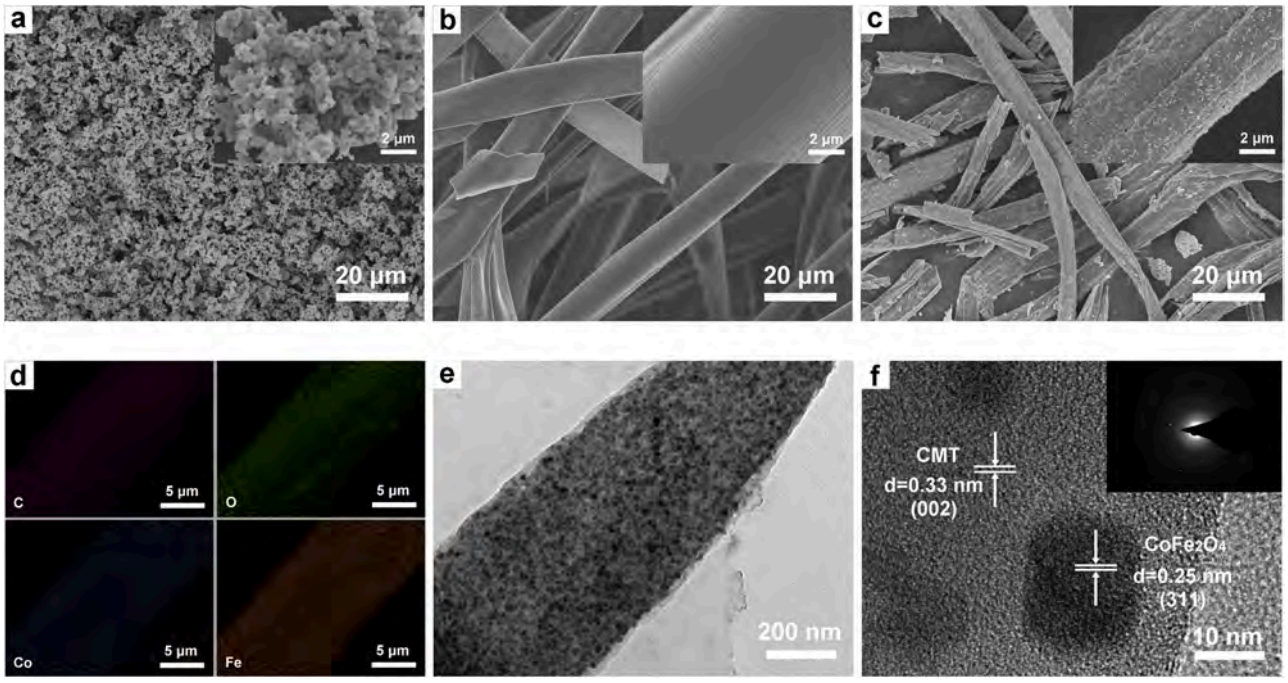

Fig. 4. SEM images of (a) $CoFe_2O_4$, (b) CMT, and (c) $CoFe_2O_4$ @CMT hybrids. (d) Elements mapping of the $CoFe_2O_4$ @CMT-1. (e) TEM and (f) HRTEM images of the $CoFe_2O_4$ @CMT-1(inserted: SAED pattern).

carried out to study the nanoscale structures of as-fabricated $CoFe_2O_4$ @CMT-1 (Fig. 4e), where $CoFe_2O_4$ nanoparticles with uniform size are homogenously immobilized to the CMT without substantial aggregations. In addition, the well-resolved lattice fringe spacing of the (311) crystalline plane for $CoFe_2O_4$ in the HRTEM (Fig. 4f) is about 0.25 nm, which is agree with the XRD results (Fig. 2a) (Wang et al., 2020b). Meanwhile, several subtle crystal lattices with d-spacing values of 0.33 nm are also observed, implying that there are crystalline regions with short-range orientations in CMT. This further confirms that the anchored $CoFe_2O_4$ nanocrystals can act as catalysts further boost the generation of graphited carbon in CMT (Qiu et al., 2017). Additionally, the electron diffraction pattern of $CoFe_2O_4$ @CMT-1 further confirms the coexistence of $CoFe_2O_4$ and CMT, evidenced by well-defined diffraction spots of crystalline planes for $CoFe_2O_4$ and CMT.

As is well known, reflection loss (RL) in terms of transmission line theory is employed to evaluate the microwave-absorbing property of a microwave absorber, which can be calculated as (Zeng et al., 2020):

$$RL = 20 \lg \left| \frac{Z_{in} - Z_0}{Z_{in} + Z_0} \right|$$

$$Z_{in} = Z_0 \sqrt{\frac{\mu_r}{\varepsilon_r}} \tanh\left(j \frac{2\pi f d}{c} \sqrt{\mu_r \varepsilon_r} \right)$$

where Z_{in} denotes the input impedance of the absorber, Z_0 denotes the impedance of free space (377 Ω), ε_r presents the relative complex permittivity, μ_r presents the relative complex permeability, f signifies the frequency of the electromagnetic wave, d is the thickness of absorber, and c is the light velocity in the free space. Typically, a lower RL value indicates a more robust absorption capacity. Moreover, EAB as a vital indicator for practical application is designated as the relevant width of the absorption frequency with RL≤ −10 dB, indicating that over 90% of electromagnetic waves can be attenuated over this frequency range.

Fig. 5a-f three-dimensionally depict RLs of as-obtained samples with thickness ranging from 1.0 mm to 5.5 mm with a step size of 0.1 mm, where the matching frequency (f_m) corresponding to minimum reflection loss (RL_{min}) shifts to lower frequency with the increase of thickness. This tendency can be interpreted with the quarter-wavelength decay formula $f_m = c/(2\pi\mu''d)$, where f_m is inversely proportional to the thickness due to the invariable mass concentration of the magnetic component in a given hybrid (Zhao et al., 2018). In order to further clarify composition-tuned microwave attenuation characteristics, the RLs at the optimized thickness of all samples were extracted and presented in Fig. 5g. With the thickest optical thickness of 5.5 mm, the RL_{min} of CMT and $CoFe_2O_4$ are only − 10.88 dB at 7.60 GHz and − 11.84 dB at 18.00 GHz, respectively, indicating that the microwave attenuation capacity of single CMT or $CoFe_2O_4$ is not enough to satisfy the criterion of practical applications. As anticipated, combining $CoFe_2O_4$ and CMT endows hybrids with improved microwave-absorbing performance. For instance, $CoFe_2O_4$ @CMT-0.5 exhibits a lower RL_{min} of –16.47 dB at 17.44 GHz with a thickness of only 1.40 mm. Remarkably, the RL_{min} of $CoFe_2O_4$ @CMT peaks at − 66.78 dB when with the ratio of $CoFe_2O_4$/CMT increases to 1, which is 6.14 times and 5.64 times than that of CMT and $CoFe_2O_4$, respectively. Although further increased $CoFe_2O_4$ deteriorates the microwave absorbing performance of $CoFe_2O_4$ @CMT hybrids, RL_{min} values of − 44.97 dB and − 41.85 dB can be obtained for $CoFe_2O_4$ @CMT-3 and $CoFe_2O_4$ @CMT-5, respectively. It can be deduced that hierarchical structures with synergetic effects of $CoFe_2O_4$ and CMT contributes to the superior RL_{min} of the resulting hybrids. Besides, for a low RL as possible, the EAB of a microwave absorber should be as broad as possible to ensure effective absorption over various frequencies. Noticeably, the EAB regions enclosed by gray lines expand due to the coexistence of $CoFe_2O_4$ and CMT (Fig. 5c-f). As shown in Fig. 5h, the EAB of CMT is only 1.28 GHz (7.04–8.32 GHz) at 5.5 mm, while sole $CoFe_2O_4$ also demonstrates an extremely low EBA of 0.64 GHz (17.36–18.00 GHz). As expected, the EAB of $CoFe_2O_4$ @CMT-0.5 is up to 4.80 GHz with thinner thickness of only 1.6 mm, almost covering the whole Ku band. Furthermore, all $CoFe_2O_4$ @CMT hybrids show an EAB higher than 4.00 GHz, demonstrating a feature of broadband absorption. In addition, the frequency range of > 90% attenuation is 3.04–18.00 GHz for $CoFe_2O_4$ @CMT-0.5 when its thickness ranges from 1.2 to 5.0 mm, implying that its EBA covers almost C, X, and Ku bands just via simply tuning the thickness, which is of great importance to broad attenuation. Fig. 5i summarizes typical

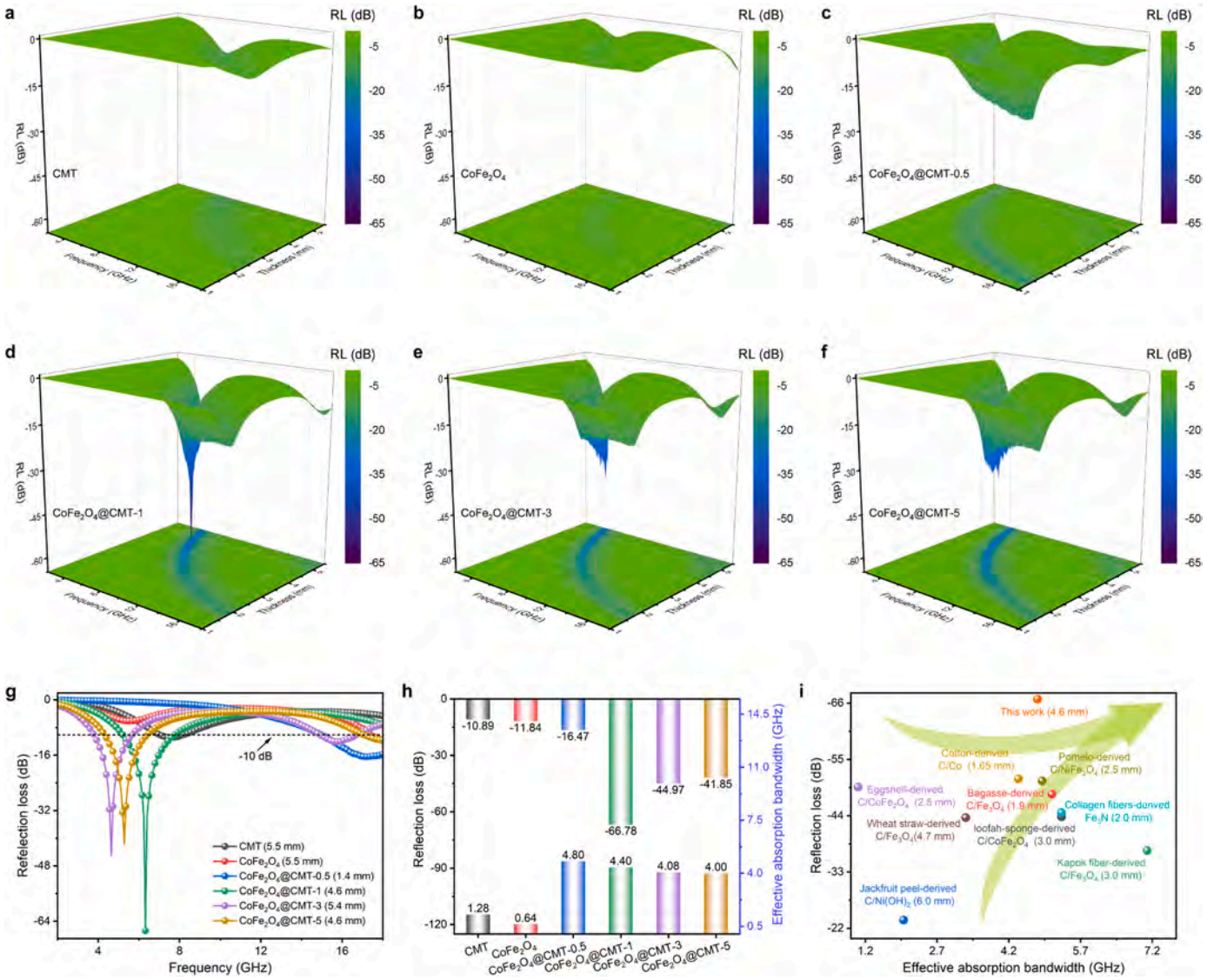

Fig. 5. (a-f) Three-dimensional mapping of RLs, (g) RL curves at optimized thickness and (h) RL_{min} as well as effective absorption bandwidth of CMT, $CoFe_2O_4$ and $CoFe_2O_4$ @CMT hybrids; (i) Microwave absorbing performance of biomass-based hybrids.

biomass-derived carbon hybrids (in wax) and their corresponding microwave-absorbing performances reported in recent publications (Ding et al., 2022; Gou et al., 2019; Guan et al., 2018; Huang et al., 2019; Liu et al., 2019a; Liu et al., 2019b; Wang et al., 2015; Wang et al., 2019; Zhao et al., 2018). In terms of comprehensive performance, $CoFe_2O_4$ @CMT hybrids in our work offer competitive advantages due to their strong absorption, broad bandwidth, and low-density, indicating that the construction of hierarchical structures with the hybridization of 0D ferrite nanoparticles and 1D hollow carbon microtube is a versatile strategy to fabricate sustainable microwave absorbers.

To elucidate insights into the synergistic influence of hierarchical dielectric/magnetic structures on microwave absorption performance, complex permittivity ($\varepsilon_r = \varepsilon' - j\varepsilon''$) and complex permeability ($\mu_r = \mu' - j\mu''$) of all samples were analyzed over the frequency ranging from 2 GHz to18 GHz. In general, the storage capability of electric/magnetic energy for a microwave absorber is associated with real parts (ε' and μ'), while the dissipation ability of electric/magnetic is related to imaginary parts (ε'' and μ''), respectively. The dielectric/magnetic loss tangent ($\tan\delta_\varepsilon = \varepsilon''/\varepsilon'$ and $\tan\delta_\mu = \mu''/\mu'$) stands for the corresponding dielectric/magnetic dissipation capability. Fig. 6a-c displays the frequency-depended ε', ε'' and $\tan\delta_\varepsilon$ for all specimen. Noteworthily, the values of ε' and ε'' $CoFe_2O_4$ @CMT hybrids exhibit a downward trend when the frequency increase, especially for $CoFe_2O_4$ @CMT-0.5 with a higher proportion of CMT, which is ascribed to the polarization lagging (Pan et al., 2023). In the high-frequency region, orientations and rearrangement of dipoles existing in the hybrids fell behind the alternation of electromagnetic wave field, resulting in decreasing ε' and ε''. It is obvious that values of ε' and ε'' are both enhanced in hybrids compared with sole CMT and $CoFe_2O_4$. Take the $CoFe_2O_4$ @CMT-0.5 for example, the average values of ε' and ε'' elevate to 9.81 and 5.88, respectively. Notably, with ε' values above 10 almost over the whole involved frequency (2.00–17.52 GHz), $CoFe_2O_4$ @CMT-0.5 demonstrates the highest electric energy storage capacity. Fig. 6c depicts $\tan\delta_\varepsilon$ as a function of frequency for all samples, where the $\tan\delta_\varepsilon$ is enhanced when dielectric and magnetic lossy components are combined, indicating more significant dielectric loss capacity and therefore microwave-absorbing performance. As shown in Fig. 6d-f, CMT offers small μ', μ'' and $\tan\delta_\mu$ around 0 with slight fluctuations due to its nonmagnetic characteristic. On the contrary, the $CoFe_2O_4$ presents the biggest values of μ', μ'', and $\tan\delta_\mu$ among the six samples, indicating its most robust attenuation capability for magnetic energy. With the increasing of $CoFe_2O_4$, the μ', μ'', and $\tan\delta_\mu$ of $CoFe_2O_4$ @CMT increase from 0.99–1.14, 0.01–0.10, and 0.01–0.09 for the $CoFe_2O_4$ @CMT-0.5 to 1.00–1.36, 0.06–0.23, and 0.05–0.18 for the $CoFe_2O_4$ @CMT-5, respectively. Compared to pure $CoFe_2O_4$ and CMT,

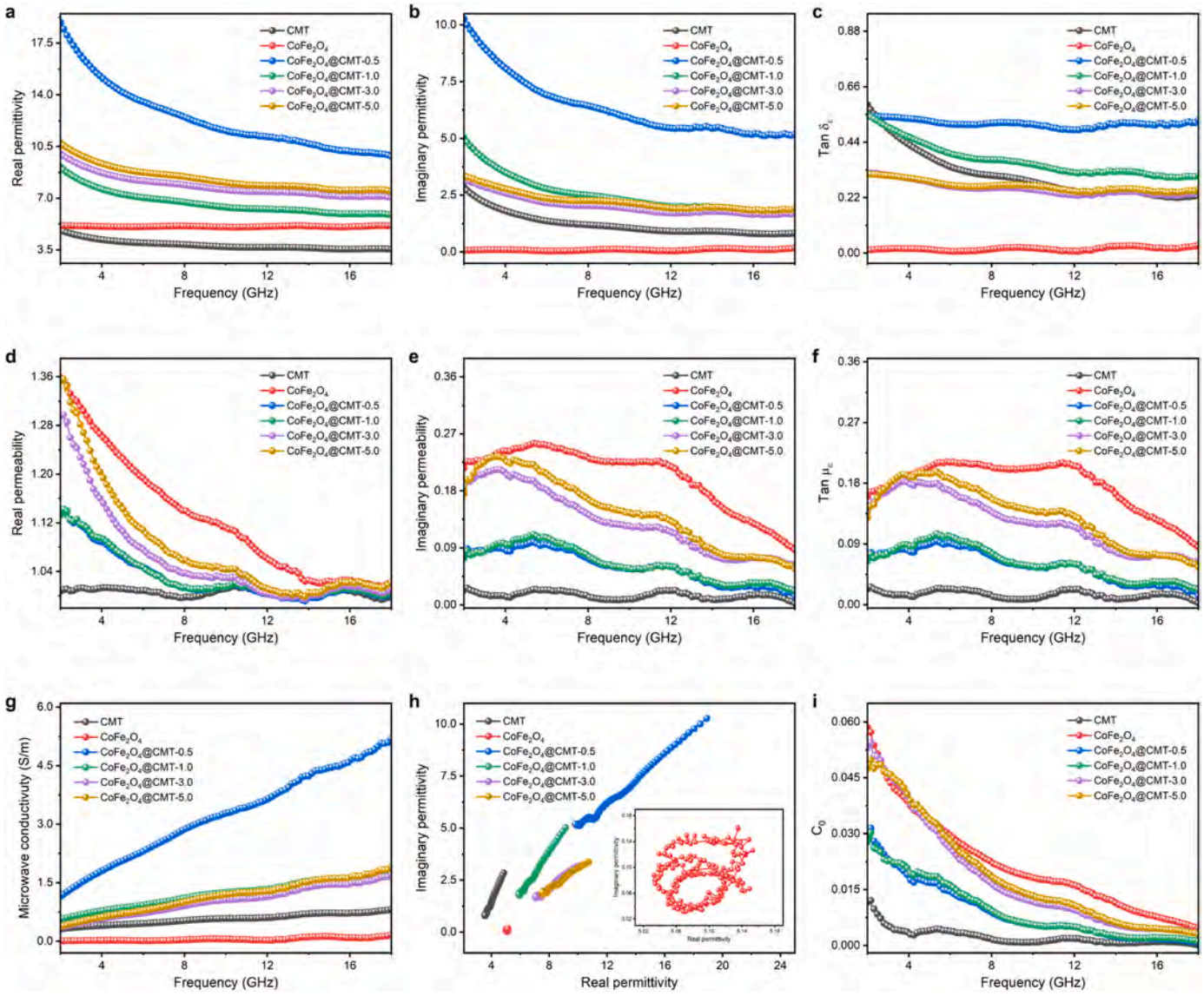

Fig. 6. Frequency-depended (a) real and (b) imaginary permittivity, (c) dielectric loss, (d) real and (e) imaginary permeability, (f) magnetic loss, (g) conductivity in microwave, (h) Cole-Cole curves and (i) eddy current loss (C_0) of CMT, $CoFe_2O_4$, and $CoFe_2O_4$ @CMT hybrids with different components.

$CoFe_2O_4$ @CMT present intermediate values of μ', μ'' and $\tan\delta_\mu$, suggesting that its magnetic loss ability is mainly stemmed from $CoFe_2O_4$. Compared with the dielectric loss-dominated attenuation capacity for CKF in our previous work (Zhao et al., 2022), $CoFe_2O_4$ @CMT hybrids in this work exhibit a balanced electromagnetic parameters, which is favorable for better impedance matching.

Generally, the microwave attenuation capacity of an absorber is mainly stemmed from the synergistic effects of multiple electromagnetic coupling. Typically, the dielectric loss is dominated by conduction loss and polarization loss. Calculated from the dielectric permittivity and dielectric loss by the equation $\sigma_{ac} = 2\pi f\varepsilon_0\varepsilon''$, the frequency-dependent microwave conductivities at room temperature for all specimen are presented in Fig. 6g, where microwave conductivity of all the composite ascend with the increasing frequency, attributing to the increased active migrating/hopping electrons and their drifted mobility at a higher frequency. Profiting from the 3D $CoFe_2O_4$ @CMT macroscopic network with many physical contacts, active sites and micro-capacitance, the incident electromagnetic energy can be efficiently transformed into other forms of energy via conduction loss. As discussed above, the coexistence of $CoFe_2O_4$ and CMT in hybrids generates enormous interfaces, resulting in multiple interfacial polarization loss because of the accumulated charges at the interfaces. In addition, CMT contains substantial defects and oxygen groups, which boosts interfacial polarization and electronic dipole relaxation due to the increased charge separation at oxygen-vacancy defect sites in hybrids (Su et al., 2022). Following the Debye theory, Cole-Cole semicircles are adopted to elaborate the relaxation process and defined as [37]:

$$\left(\varepsilon' - \frac{\varepsilon_s - \varepsilon_\infty}{2}\right)^2 + \varepsilon'' = \left(\frac{\varepsilon_s - \varepsilon_\infty}{2}\right)^2$$

Herein, ε_s denotes the static permittivity, and ε_∞ is the relative dielectric permittivity at infinite frequency. As the Cole-Cole curves shown in Fig. 6**h**, there are 0, 3, and 4 distorted semicircles in the curves of $CoFe_2O_4$, CMT, and $CoFe_2O_4$ @CMT hybrids, which indicates that $CoFe_2O_4$ @CMT hybrids demonstrate more Debye relaxation processes than its counterparts, ascribing to carbonization-induced defects and abundant components-derived heterogeneous interfaces (Xu et al., 2022b). Due to the lower coverage of $CoFe_2O_4$ and resistance between different hollow hybrids, the $CoFe_2O_4$ @CMT-0.5 sample presents a longer conductive loss regime than the other three hybrids, demonstrating that there are more hopping and migrating electrons in its 3D interconnected network (Gu et al., 2021). Considering the dual factors, it

is easily deduced that the best microwave attenuation capacity of $CoFe_2O_4$ @CMT-1 results from the balanced conduction loss and polarization processes. As another vital factor contributing to electromagnetic wave attenuation, magnetic loss mainly involves domain wall resonance, magnetic hysteresis loss, eddy current loss, and natural/exchange resonance (Xu et al., 2022b). Typically, domain wall resonance can be neglected here since it typically occurs at a megahertz frequency (<100 MHz) (Wang et al., 2018a). While magnetic hysteresis loss roots from the irreversible movement and displacement of the magnetic domains, eddy current loss mainly originates from electromagnetic induction in an alternating electromagnetic field (Huang et al., 2019). Compared with natural resonance occurring when the frequency equals the magnetic crystal intrinsic frequency, exchange resonance happens at a higher frequency (Liu et al., 2022). To clarify the magnetic loss characteristics of $CoFe_2O_4$ @CMT hybrids, eddy current loss ($C_0 = \mu''(\mu')^{-2}f^{-1}$) is measured and presented in Fig. 6i, where C_0 should be independent of the variation of frequency if magnetic loss merely results from eddy current loss (Chen et al., 2021). Noticeably, some significant fluctuations in low-frequency regions (2 −14 GHz) imply the presence of natural/exchange resonances.

Besides electromagnetic loss, impedance matching and attenuation capacity also contribute to microwave-absorbing performances, which is estimated by impedance matching degree ($|Z|$) and attenuation constant (α). According to the transmission line theory, $|Z|$ and α can be calculated as (Zeng et al., 2020):

$$Z = |Z_{in}/Z_0| = \sqrt{\frac{\mu_r}{\varepsilon_r}}\tanh\left(j\frac{2\pi fd}{c}\sqrt{\mu_r\varepsilon_r}\right)$$

$$\alpha = \frac{\sqrt{2}\pi f}{c}\sqrt{\left(\mu''\varepsilon'' - \mu'\varepsilon'\right) + \sqrt{(\mu''^2 + \mu'^2)(\varepsilon''^2 + \mu''^2)}}$$

Impedance matching reflects the ability of allowing electromagnetic energy entering microwave absorbers, requiring a balance between complex permeability and permittivity (Liu et al., 2020). Fig. 7a-f shows the calculated $|Z|$ contour plots of $CoFe_2O_4$, CMT, and $CoFe_2O_4$ @CMT, where the closer Z to 1 means the better impedance matching characteristic. As seen in Fig. 7c, $|Z|$ values of $CoFe_2O_4$ @CMT-0.5 are below 0.8 over the involved thickness and frequency, suggesting poor impedance matching and inferior RL characteristics. From Fig. 7d-f, the domain with $|Z|$ values of 0.8–1.2 for $CoFe_2O_4$ @CMT-1, $CoFe_2O_4$ @CMT-3, and $CoFe_2O_4$ @CMT-5 are bigger than that of $CoFe_2O_4$, CMT, and $CoFe_2O_4$ @CMT-0.5, thus resulting better impedance matching and superior RL characteristics. Attenuation constant presents the capacity to dissipate penetrated electromagnetic energy. Fig. 7g displays the

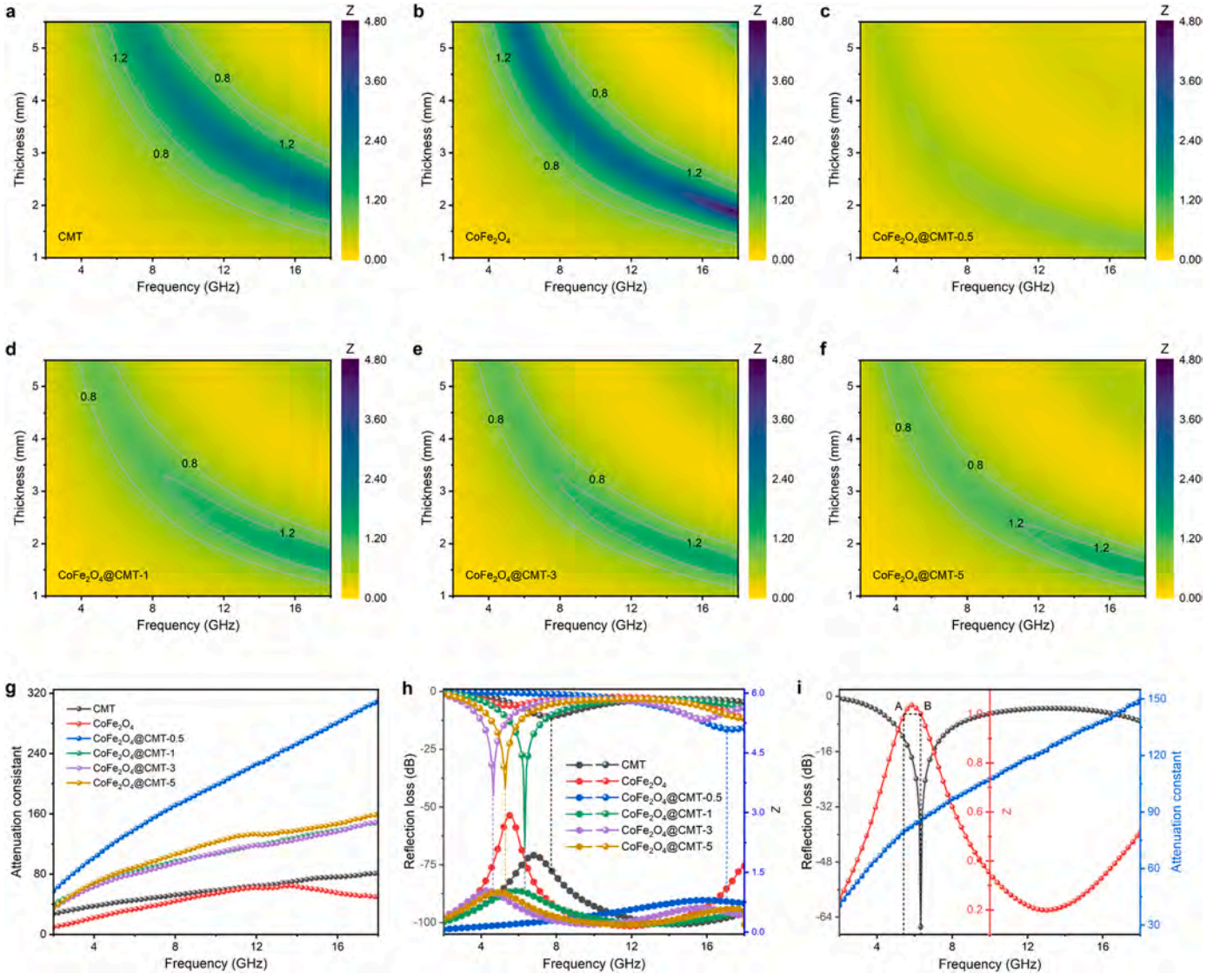

Fig. 7. (a-f) Contour plots of $|Z|$ values, (g) attenuation constant, and (h) $|Z|$ vs. RLof CMT, $CoFe_2O_4$, and $CoFe_2O_4$ @CMT hybrids; (i) frequency dependence of RL, Z values and attenuation constant for $CoFe_2O_4$ @CMT-1.

attenuation constant α of CMT, $CoFe_2O_4$, and $CoFe_2O_4$ @CMT hybrids. Both sole CMT and $CoFe_2O_4$ exhibit low α values, and the higher α values of $CoFe_2O_4$ @CMT hybrids indicate improved attenuation capacity, ascribing to synergetic effects of dielectric/magnetic blocks in $CoFe_2O_4$ @CMT hybrids. Additionally, the attenuation constant of $CoFe_2O_4$ @CMT-0.5 is higher than that of other hybrids in whole frequency, indicating dielectric loss mainly attributes to its dissipation of electromagnetic energy. However, $CoFe_2O_4$ @CMT-0.5 exhibits inferior RL characteristics (Fig. 5c) due to its poor impedance matching (Fig. 7c), which verifies that excellent microwave-absorption performances are not only associated with high attenuation ability. As evidenced by Fig. 7h, RL peaks at a higher frequency rather than a lower frequency for all samples when the Z value equals 1. To find the reason behind this phenomenon, the relations among RL_{min}, Z value, and α is further analyzed (Fig. 7**i**). Owing to the growing α with the increasing frequency, point B (higher frequency) exhibits a higher α than that point A (lower frequency) dose, indicating that a higher α is favorable for obtaining a superior microwave-absorbing property if the impedance matching is same (Yang et al., 2021).

As discussed above, hierarchical structures with the synergetic effects of dielectric and magnetic networks are responsible for the balanced impedance matching degree and microwave attenuation capacity for $CoFe_2O_4$ @CMT, endowing excellent microwave-absorbing performances (Fig. 8). For the former, hierarchical structures with macroscopic networks, microscopic tubular channels, and nanoscopic pores boosts impedance matching, allowing as much incident electromagnetic energy to enter microwave absorbers as possible. When it comes to microwave attenuation capacity, the coexistence of dielectric CMT and magnetic $CoFe_2O_4$ gives hybrids improved attenuation capacity with multiple loss mechanisms. Initially, intact CMT networks offer surface/interlayer channels for electronic migrations as well as hopping, resulting in significant conduction loss. Moreover, in-situ carbonization of KF induces a larger number of defects and dipoles, which further generates high relaxation loss via dipole/relaxation polarization. Meanwhile, the introduction of $CoFe_2O_4$ tunes the impedance matching degree and offers intrinsically high magnetic dissipations in forms of hysteresis loss, eddy current loss, and natural/exchange resonance loss. Comprehensively, 3D macroscopic porous aerogels together with 1D microscopic hollow tubes generate multiple reflection/scattering and abundant heterogeneous interfaces inner trap spaces, peculiar coexistence of porous structure with the coexistence of $CoFe_2O_4$ and CMT generates, which is conducive for interfacial polarization and multiple reflection/scattering loss.

4. Conclusions

In summary, a hierarchical structure with dielectric/magnetic network was prepared by a facial approach combining the in-situ solvothermal synthesis of $CoFe_2O_4$ as well as carbonization of KF, and electromagnetic parameters of the as-prepared hybrid can be conveniently regulated via controlling the $CoFe_2O_4$. Profiting from hierarchical structures derived from 1D hollow microtube with dielectric and magnetic components, $CoFe_2O_4$ @CMT hybrids demonstrate superior microwave absorbing performances. The optimized reflection loss of the $CoFe_2O_4$ @CMT peaks − 66.78 dB at 4.6 mm, and its effective absorption bandwidth is up to 4.80 GHz, primarily ascribing to good impedance matching conditions resulting from hierarchical structures of 1D hollow microtube and improved microwave attenuation capacity with multiple loss mechanisms derived from the synergic effects of dielectric and magnetic lossy blocks. This work opens a promising pathway for developing biomass-based hybrid materials with novel heterogeneous structures toward excellent microwave absorption materials.

CRediT authorship contribution statement

Pengfei Zhao: Investigation, Writing – original draft, Funding acquisition. **Rui Wang:** Data curation, Formal analysis. **Jinlong Tao:** Formal analysis, Funding acquisition. **Ximei Song:** Resources, Formal analysis, Writing – review & editing. **Yanfang Zhao:** Data curation, Formal analysis. **Jianhe Liao:** Formal analysis, Writing – review & editing. **Lusheng Liao:** Data curation, Funding acquisition. **Zheng Peng:** Conceptualization, Project administration.

Declaration of Competing Interest

The authors declare that they have no known competing financial

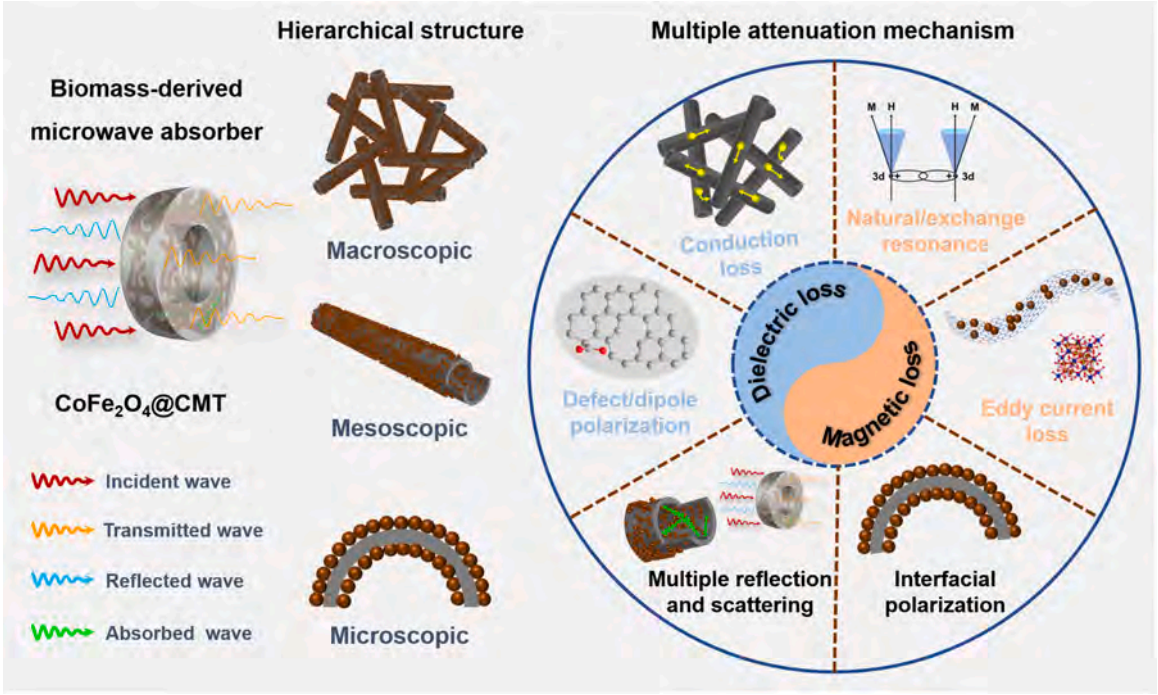

Fig. 8. Schematic description of the proposed microwave attenuation mechanisms for hierarchical $CoFe_2O_4$ @CMT hybrids.

interests or personal relationships that could have appeared to influence the work reported in this paper.

Data availability

Data will be made available on request.

Acknowledgments

This work was supported by the Natural Science Foundation of Guangdong Province (2022A1515010936), the National Key Research and Development Program of China (2022YFD2301203), Key Research and Development Project of Hainan Province (ZDYF2022GXJS226), and the Central Public-interest Scientific Institution Basal Research Fund for Chinese Academy of Tropical Agricultural Sciences (1630122022007).

References

Bao, S., Song, Z., Mao, R., Li, Y., Zhang, S., Jiang, Z., Li, X., Xie, Z., 2021. Synthesis of hollow rod-like hierarchical structures assembled by CoFe/C nanosheets for enhanced microwave absorption. J. Mater. Chem. C. 9, 13860–13868.

Chen, J., Zheng, J., Huang, Q., Wang, F., Ji, G., 2021. Enhanced microwave absorbing ability of carbon fibers with embedded FeCo/CoFe(2)O(4) nanoparticles. ACS Appl. Mater. Interfaces 13, 36182–36189.

Cui, X., Liu, W., Gu, W., Liang, X., Ji, G., 2019. Two-dimensional MoS2 modified using CoFe2O4 nanoparticles with enhanced microwave response in the X and Ku band. Inorg. Chem. Front. 6, 590–597.

Ding, C., Fu, H., Wu, T., Tang, Y., Hu, X., Wu, S., Zhang, L., Wen, G., Huang, X., 2022. Heterogeneous network constructed by high aspect-ratio Kapok biomass microtube for lightweight and broadband microwave absorbent. Carbon 191, 424–432.

Fang, J., Shang, Y., Chen, Z., Wei, W., Hu, Y., Yue, X., Jiang, Z., 2017. Rice husk-based hierarchically porous carbon and magnetic particles composites for highly efficient electromagnetic wave attenuation. J. Mater. Chem. C. 5, 4695–4705.

Geng, H., Guo, Y., Zhang, X., Zhang, Y., Wang, X., Zhao, P., Wang, G., Liao, J., Dong, L., 2023. Combination strategy of large interlayer spacing and active basal planes for regulating the microwave absorption performance of MoS2/MWCNT composites at thin absorber level. J. Colloid Interface Sci. 648, 12–24.

Gou, G., Meng, F., Wang, H., Jiang, M., Wei, W., Zhou, Z., 2019. Wheat straw-derived magnetic carbon foams: in-situ preparation and tunable high-performance microwave absorption. Nano Res. 12, 1423–1429.

Gu, W., Sheng, J., Huang, Q., Wang, G., Chen, J., Ji, G., 2021. Environmentally friendly and multifunctional shaddock peel-based carbon aerogel for thermal-insulation and microwave absorption. Nanomicro Lett. 13, 102.

Guan, H., Wang, H., Zhang, Y., Dong, C., Chen, G., Wang, Y., Xie, J., 2018. Microwave absorption performance of Ni(OH)(2) decorating biomass carbon composites from Jackfruit peel. Appl. Surf. Sci. 447, 261–268.

Han, L.Y., Li, K.Z., Fu, Y.Q., Yin, X.M., Jiao, Y.M., Song, Q., 2022. Carbon microtube/NiCo carbonate hydride nanoneedle composite foams for broadband electromagnetic interference shielding. Acs Appl. Nano Mater. 5, 4082–4090.

Huang, L., Li, J., Wang, Z., Li, Y., He, X., Yuan, Y., 2019. Microwave absorption enhancement of porous C@CoFe2O4 nanocomposites derived from eggshell membrane. Carbon 143, 507–516.

Huang, W., Tong, Z., Wang, R., Liao, Z., Bi, Y., Chen, Y., Ma, M., Lyu, P., Ma, Y., 2020. A review on electrospinning nanofibers in the field of microwave absorption. Ceram. Int. 46, 26441–26453.

Huang, X., Lu, M., Zhang, X., Wen, G., Zhou, Y., Fei, L., 2012. Carbon microtube/Fe3O4 nanocomposite with improved wave-absorbing performance. Scr. Mater. 67, 613–616.

Huang, X., Yan, X., Xia, L., Wang, P., Wang, Q., Zhang, X., Zhong, B., Zhao, H., Wen, G., 2016. A three-dimensional graphene/Fe3O4/carbon microtube of sandwich-type architecture with improved wave absorbing performance. Scr. Mater. 120, 107–111.

Jin, C., Wu, Z., Zhang, R., Qian, X., Xu, H., Che, R., 2021. 1D electromagnetic-gradient hierarchical carbon microtube via coaxial electrospinning design for enhanced microwave absorption. ACS Appl. Mater. Interfaces 13, 15939–15949.

Li, X., Wang, L., You, W., Xing, L., Yang, L., Yu, X., Zhang, J., Li, Y., Che, R., 2019. Enhanced polarization from flexible hierarchical MnO2 arrays on cotton cloth with excellent microwave absorption. Nanoscale 11, 13269–13281.

Liu, L., Yang, S., Hu, H., Zhang, T., Yuan, Y., Li, Y., He, X., 2019a. Lightweight and efficient microwave-absorbing materials based on loofah-sponge-derived hierarchically porous carbons. ACS Sustain. Chem. Eng. 7, 1228–1238.

Liu, Y., Chen, Z., Xie, W., Song, S., Zhang, Y., Dong, L., 2019b. In-situ growth and graphitization synthesis of porous Fe3O4/carbon fiber composites derived from biomass as lightweight microwave absorber. ACS Sustain. Chem. Eng. 7, 5318–5328.

Liu, P., Gao, S., Chen, C., Zhou, F., Meng, Z., Huang, Y., Wang, Y., 2020. Vacancies-engineered and heteroatoms-regulated N-doped porous carbon aerogel for ultrahigh microwave absorption. Carbon 169, 276–287.

Liu, T., Huang, L., Wang, X., Yuan, Y., 2022. Multifunctional Nd2O3/CNFs composite for microwave absorption and anti-corrosion applications. ACS Appl. Electron. Mater.

Lv, H., Yang, Z., Pan, H., Wu, R., 2022. Electromagnetic absorption materials: current progress and new frontiers. Prog. Mater. Sci. 127, 100946.

Meng, F.B., Wang, H.G., Huang, F., Guo, Y.F., Wang, Z.Y., Hui, D., Zhou, Z.W., 2018. Graphene-based microwave absorbing composites: a review and prospective. Compos. Part B-Eng. 137, 260–277.

Pan, F., Ning, M., Li, Z., Batalu, D., Guo, H., Wang, X., Wu, H., Lu, W., 2023. Sequential architecture induced strange dielectric-magnetic behaviors in ferromagnetic microwave absorber. Adv. Funct. Mater. 33, 2300374..

Pang, H.F., Duan, Y.P., Huang, L.X., Song, L.L., Liu, J., Zhang, T., Yang, X., Liu, J.Y., Ma, X.R., Di, J.R., Liu, X.J., 2021. Research advances in composition, structure and mechanisms of microwave absorbing materials. Compos Part B-Eng. 224, 109173.

Qiu, X., Wang, L., Zhu, H., Guan, Y., Zhang, Q., 2017. Lightweight and efficient microwave absorbing materials based on walnut shell-derived nano-porous carbon. Nanoscale 9, 7408–7418.

Ren, F.J., Yu, H.J., Wang, L., Saleem, M., Tian, Z.F., Ren, P.F., 2014. Current progress on the modification of carbon nanotubes and their application in electromagnetic wave absorption. RSC Adv. 4, 14419–14431.

Sharma, G.K., James, N.R., 2021. Progress in electrospun polymer composite fibers for microwave absorption and electromagnetic interference shielding. ACS Appl. Electron. Mater. 3, 4657–4680.

Song, P., Cui, J., Di, J., Liu, D., Xu, M., Tang, B., Zeng, Q., Xiong, J., Wang, C., He, Q., Kang, L., Zhou, J., Duan, R., Chen, B., Guo, S., Liu, F., Shen, J., Liu, Z., 2020. Carbon microtube aerogel derived from kapok fiber: an efficient and recyclable sorbent for oils and organic solvents. ACS Nano 14, 595–602.

Song, S., Li, H., Liu, P., Peng, X., 2022. Applications of cellulose-based composites and their derivatives for microwave absorption and electromagnetic shielding. Carbohydr. Polym. 287, 119347.

Su, Z., Zhang, W., Lu, J., Tian, L., Yi, S., Zhang, Y., Zhou, S., Niu, B., Long, D., 2022. Oxygen-vacancy-rich Fe3O4/carbon nanosheets enabling high-attenuation and broadband microwave absorption through the integration of interfacial polarization and charge-separation polarization. J. Mater. Chem. A 10, 8479–8490.

Sun, J., Wu, Z., Ma, C., Xu, M., Luo, S., Li, W., Liu, S., 2021. Biomass-derived tubular carbon materials: progress in synthesis and applications. J. Mater. Chem. A 9, 13822–13850.

Wang, G., Ong, S.J.H., Zhao, Y., Xu, Z.J., Ji, G., 2020a. Integrated multifunctional macrostructures for electromagnetic wave absorption and shielding. J. Mater. Chem. A 8, 24368–24387.

Wang, X.Y., Lu, Y.K., Zhu, T., Chang, S.C., Wang, W., 2020b. CoFe2O4/N-doped reduced graphene oxide aerogels for high-performance microwave absorption. Chem. Eng. J. 388, 124317.

Wang, H., Meng, F., Li, J., Li, T., Chen, Z., Luo, H., Zhou, Z., 2018a. Carbonized design of hierarchical porous carbon/Fe3O4@Fe derived from loofah sponge to achieve tunable high-performance microwave absorption. ACS Sustain. Chem. Eng. 6, 11801–11810.

Wang, Z., Zhao, P., He, D., Cheng, Y., Liao, L., Li, S., Luo, Y., Peng, Z., Li, P., 2018b. Cerium oxide immobilized reduced graphene oxide hybrids with excellent microwave absorbing performance. Phys. Chem. Chem. Phys. 20, 14155–14165.

Wang, W., Wang, F., Kang, Y., Wang, A., 2014. Au nanoparticles decorated Kapok fiber by a facile noncovalent approach for efficient catalytic decoloration of Congo Red and hydrogen production. Chem. Eng. J. 237, 336–343.

Wang, X., Huang, X., Chen, Z., Liao, X., Liu, C., Shi, B., 2015. Ferromagnetic hierarchical carbon nanofiber bundles derived from natural collagen fibers: truly lightweight and high-performance microwave absorption materials. J. Mater. Chem. C. 3, 10146–10153.

Wang, Y., Gao, X., Zhou, H.W., Wu, X.M., Zhang, W.Z., Wang, Q.G., Luo, C.Y., 2019. Fabrication of biomass-derived carbon decorated with NiFe2O4 particles for broadband and strong microwave absorption. Powder Technol. 345, 370–378.

Wongkasem, N., 2021. Electromagnetic pollution alert: Microwave radiation and absorption in human organs and tissues. Electromagn. Biol. Med. 40, 236–253.

Wu, Z., Tian, K., Huang, T., Hu, W., Xie, F., Wang, J., Su, M., Li, L., 2018. Hierarchically porous carbons derived from biomasses with excellent microwave absorption performance. ACS Appl. Mater. Interfaces 10, 11108–11115.

Xie, W., Cheng, H.F., Chu, Z.Y., Chen, Z.H., 2008. Microwave absorbing properties of short hollow carbon fiber composites. J. Inorg. Mater. 23, 481–485.

Xu, C., Liu, P., Wu, Z., Zhang, H., Zhang, R., Zhang, C., Wang, L., Wang, L., Yang, B., Yang, Z., You, W., Che, R., 2022a. Customizing heterointerfaces in multilevel hollow architecture constructed by magnetic spindle arrays using the polymerizing-etching strategy for boosting microwave absorption. Adv. Sci. 9, e2200804.

Xu, R., Xu, D., Zeng, Z., Liu, D., 2022b. CoFe2O4/porous carbon nanosheet composites for broadband microwave absorption. Chem. Eng. J. 427, 130796.

Xu, M., Li, J., Yan, Y., Zhao, X., Yan, J., Zhang, Y., Lai, B., Chen, X., Song, L., 2019. Catalytic degradation of sulfamethoxazole through peroxymonosulfate activated with expanded graphite loaded CoFe2O4 particles. Chem. Eng. J. 369, 403–413.

Yang, X., Pang, X., Cao, M., Liu, X., Li, X., 2021. Efficient microwave absorption induced by hierarchical pores of reed-derived ultralight carbon materials. Ind. Crops Prod. 171, 113814.

Yu-Rui, Z., Bing-Chang, W., Shi-Long, G., Li-Peng, Q., Quan-Hao, Z., Guo-Ting, C., Wen-Peng, H., Seeram, R., Yun-Ze, L., 2022. Electrospun MXene nanosheet/polymer composites for electromagnetic shielding and microwave absorption: a review. ACS Appl. Nano Mater.

Zeng, X., Cheng, X., Yu, R., Stucky, G.D., 2020. Electromagnetic microwave absorption theory and recent achievements in microwave absorbers. Carbon 168, 606–623.

Zhao, H., Cheng, Y., Ma, J., Zhang, Y., Ji, G., Du, Y., 2018. A sustainable route from biomass cotton to construct lightweight and high-performance microwave absorber. Chem. Eng. J. 339, 432–441.

Zhao, H., Cheng, Y., Liu, W., Yang, L., Zhang, B., Wang, L.P., Ji, G., Xu, Z.J., 2019. Biomass-derived porous carbon-based nanostructures for microwave absorption. Nanomicro Lett. 11, 24.

Zhao, Y., Long, A., Zhao, P., Liao, L., Wang, R., Li, G., Wang, B., Liao, X., Yu, R., Liao, J., 2022. Natural hollow fiber-derived carbon microtube with broadband microwave attenuation capacity. Polymers 14, 4501.
Zheng, Y., Song, Y., Gao, T., Yan, S., Hu, H., Cao, F., Duan, Y., Zhang, X., 2020. Lightweight and hydrophobic three-dimensional wood-derived anisotropic magnetic porous carbon for highly efficient electromagnetic interference shielding. ACS Appl. Mater. Interfaces 12, 40802–40814.
Zheng, Y., Wang, J., Wang, A., 2021. Recent advances in the potential applications of hollow kapok fiber-based functional materials. Cellulose 28, 5269–5292.
Zhi, D., Li, T., Li, J., Ren, H., Meng, F., 2021. A review of three-dimensional graphene-based aerogels: Synthesis, structure and application for microwave absorption. Compos. Part B: Eng. 211, 108642.
Zhou, M., Gu, W., Wang, G., Zheng, J., Pei, C., Fan, F., Ji, G., 2020. Sustainable wood-based composites for microwave absorption and electromagnetic interference shielding. J. Mater. Chem. A 8, 24267–24283.